Draft version August 4, 2014
Preprint typeset using LaTeX style emulateapj v. 5/2/11

HIGH-ENERGY X-RAY IMAGING OF THE PULSAR WIND NEBULA MSH 15−52: CONSTRAINTS ON PARTICLE ACCELERATION AND TRANSPORT

Hongjun An[1], Kristin K. Madsen[2], Stephen P. Reynolds[3], Victoria M. Kaspi[1], Fiona A. Harrison[2], Steven E. Boggs[4], Finn E. Christensen[5], William W. Craig[4,6], Chris L. Fryer[7], Brian W. Grefenstette[2], Charles J. Hailey[8], Kaya Mori[8], Daniel Stern[9], and William W. Zhang[10]

[1]Department of Physics, McGill University, Montreal, Quebec, H3A 2T8, Canada
[2]Cahill Center for Astronomy and Astrophysics, California Institute of Technology, Pasadena, CA 91125, USA
[3]Physics Department, NC State University, Raleigh, NC 27695, USA
[4]Space Sciences Laboratory, University of California, Berkeley, CA 94720, USA
[5]DTU Space, National Space Institute, Technical University of Denmark, Elektrovej 327, DK-2800 Lyngby, Denmark
[6]Lawrence Livermore National Laboratory, Livermore, CA 94550, USA
[7]CCS-2, Los Alamos National Laboratory, Los Alamos, NM 87545, USA
[8]Columbia Astrophysics Laboratory, Columbia University, New York NY 10027, USA
[9]Jet Propulsion Laboratory, California Institute of Technology, Pasadena, CA 91109, USA
[10]Goddard Space Flight Center, Greenbelt, MD 20771, USA

Draft version August 4, 2014

ABSTRACT

We present the first images of the pulsar wind nebula (PWN) MSH 15−52 in the hard X-ray band ($\gtrsim$8 keV), as measured with the *Nuclear Spectroscopic Telescope Array (NuSTAR)*. Overall, the morphology of the PWN as measured by *NuSTAR* in the 3–7 keV band is similar to that seen in *Chandra* high-resolution imaging. However, the spatial extent decreases with energy, which we attribute to synchrotron energy losses as the particles move away from the shock. The hard-band maps show a relative deficit of counts in the northern region towards the RCW 89 thermal remnant, with significant asymmetry. We find that the integrated PWN spectra measured with *NuSTAR* and *Chandra* suggest that there is a spectral break at 6 keV which may be explained by a break in the synchrotron-emitting electron distribution at ∼200 TeV and/or imperfect cross calibration. We also measure spatially resolved spectra, showing that the spectrum of the PWN softens away from the central pulsar B1509−58, and that there exists a roughly sinusoidal variation of spectral hardness in the azimuthal direction. We discuss the results using particle flow models. We find non-monotonic structure in the variation with distance of spectral hardness within 50″ of the pulsar moving in the jet direction, which may imply particle and magnetic-field compression by magnetic hoop stress as previously suggested for this source. We also present 2-D maps of spectral parameters and find an interesting shell-like structure in the $N_{\rm H}$ map. We discuss possible origins of the shell-like structure and their implications.

Subject headings: ISM: supernova remnants – ISM: individual (G320.4−1.2) – ISM: jets and outflows – X-rays: ISM – stars: neutron – pulsars: individual (PSR B1509−58)

1. INTRODUCTION

A pulsar wind nebula (PWN) is a region of particles accelerated in a shock formed by the interaction between the pulsar's particle/magnetic flux and ambient matter such as a supernova remnant (SNR) or the interstellar medium (ISM). It has been theorized that the shock, called a termination shock, can accelerate particles to $\sim 10^{15}$ eV, which are believed to contribute to the cosmic ray spectrum from low energies up to the 'knee' at $\sim 10^{15}$ eV (e.g., de Jager et al. 1992; Atoyan et al. 1996). In a PWN, the shock-accelerated particles propagate downstream and emit synchrotron photons under the effects of the magnetic fields in that region (Wilson 1972a,b; Rees & Gunn 1974). The electrons in the hard tail of the energy distribution produce X-rays, and thus the detection of synchrotron X-rays indirectly proves the existence of high energy electrons. Therefore, X-ray emitting PWNe are particularly interesting for studying particle shock acceleration, and for studying the interaction of high energy particles with their environments (see Gaensler & Slane 2006, for a review).

Since the accelerated particles in young PWNe lose their energy primarily via synchrotron radiation at a rate proportional to E^2, the energy distribution of the particles softens with distance from the shock, an effect called 'synchrotron burn-off'. As the particle spectrum softens, the emitted photon spectrum is expected to soften as well. Details of the softening depend on the physical environment and the particle flow in the PWNe; these have been modeled using particle advection (e.g., Kennel & Coroniti 1984; Reynolds 2003, 2009) and/or diffusion (e.g., Gratton 1972; Tang & Chevalier 2012). In particular, the advection models predict the radial profile of the photon index to be flat out to the PWN edge and then to soften rapidly, while diffusion models predict a gradual spectral softening with radius. The particle spectrum can be inferred from the photon spectrum as they are directly related. Therefore, spatially resolved spectra or energy resolved images can be compared to

Table 1
Summary of observations

Obs. No.	Observatory	Obs. ID	Exposure (ks)	Start Date (MJD)
C1	*Chandra*	754	19	51770.6
C2	*Chandra*	5534	49	53367.4
C3	*Chandra*	5535	43	53408.6
C4	*Chandra*	6116	47	53489.2
C5	*Chandra*	6117	46	53661.0
N1	*NuSTAR*	40024004002	42	56450.9
N2	*NuSTAR*	40024002001[a]	43	56451.8
N3	*NuSTAR*	40024003001	44	56452.6
N4	*NuSTAR*	40024001002	34	56519.6

Notes. All *Chandra* observations were made with the timed exposure mode (TE) on ACIS-I chips.
[a] Only used for the spectral analysis along the jet and timing analysis.

model prediction to infer the particle flow properties and the physical environments in PWNe.

MSH 15−52 (also known as "Hand of God") is a large TeV-detected PWN which is powered by the central 150-ms X-ray pulsar B1509−58 at a distance of ∼5.2 kpc (Gaensler et al. 1999). The radius of the PWN is $\sim 5'$ (∼ 7.6 pc) and it has a very asymmetric morphology with complicated internal structures in the X-ray band (e.g., Gaensler et al. 2002; DeLaney et al. 2006; Yatsu et al. 2009). Notably, it has a hard jet directed south-east, similar to that seen in some PWNe such as the Crab nebula (Mori et al. 2004). North of the PWN, there is a large thermal shell structure (RCW 89) which is thought to be powered by the PWN through finger-like structures (Yatsu et al. 2005). The synchrotron burn-off effect in this PWN was previously measured with *XMM-Newton* in the 0.5–10 keV band by Schöck et al. (2010). They measured the burn-off effect in that band by integrating the spectrum azimuthally, however, given the highly asymmetric morphology, a more in-depth analysis is warranted.

In this paper, we report on the spatial and spectral properties of the PWN MSH 15−52 in a broad X-ray band measured with *NuSTAR* and *Chandra*. We present a two-dimensional synchrotron burn-off map for the first time using energy-resolved images and spatially resolved spectra. We describe the observations and data reduction in Section 2, and show the data analysis and results in Section 3. We discuss the implications of the analysis results in Section 4 and present the summary in Section 5.

2. OBSERVATIONS

The *NuSTAR* instrument has two co-aligned hard X-ray optics and focal plane modules (modules A and B with each module having four detectors), and is the most sensitive satellite to date in the 3–79 keV band. The energy resolution is 400 eV at 10 keV (FWHM), and the temporal resolution is 2 μs (see Harrison et al. 2013, for more details), although the accuracy on orbital timescales is ∼2 ms due to long-term clock drift. *NuSTAR* has unparalleled angular resolution in the hard X-ray band (HPD=$58''$). The fine broadband angular response enables us to study detailed morphological changes with energy for large PWNe such as MSH 15−52, and *NuSTAR*'s temporal resolution is sufficient to filter out contamination from the bright central pulsar (e.g., see Chevalier 2005; Kaspi, Roberts & Harding 2006, for pulsars in PWNe).

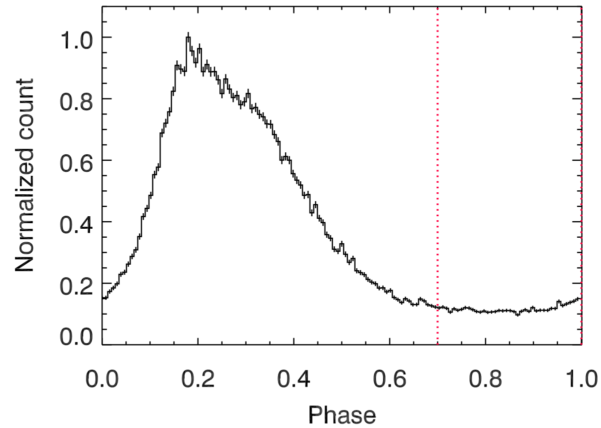

Figure 1. Normalized pulse profile for PSR B1509−58 in the 3–79 keV band measured with *NuSTAR*. Note that the off-pulse phases (0.7–1.0, dotted vertical lines) include DC emission of the pulsar as well as the nebula emission.

MSH 15−52 was observed with *NuSTAR* in 2013 July with a total net exposure of ∼160 ks. Although the *NuSTAR* field of view (FoV) is large enough to observe the whole PWN with a single pointing, we used four different pointings in order to better sample different regions of the PWN. We also analyzed archival *Chandra* ACIS (Garmire et al. 2003) observations in order to verify our spatial analysis technique, and to broaden the energy range for spectroscopy (see also Gaensler et al. 2002; DeLaney et al. 2006; Yatsu et al. 2009). Table 1 summarizes the observations used in this paper. The *NuSTAR* observation N2 was pointed to the jet, and most of the PWN fell outside the FoV. Therefore we used this observation only for the timing analysis in Section 3.1 and the spectral analysis along the jet direction in Section 3.3.3.

The *NuSTAR* data were processed with `nupipeline` 1.3.0 along with CALDB version 20131007, and the *Chandra* data were reprocessed using the `chandra_repro` tool of CIAO 4.5 along with CALDB 4.5.7. We further processed the cleaned event files for analyses as described below.

3. DATA ANALYSIS AND RESULTS

3.1. *Timing Analysis*

Since the pulsar B1509−58 is very bright, we needed to minimize its contamination in the PWN imaging and spectral analysis. For the *Chandra* data, the pulsar contamination was removed by image filtering. However, we were not able to do the image filtering for *NuSTAR* because its point spread function (PSF) is broad. Therefore, we selected the off-pulse interval in the *NuSTAR* data for the image and spectral analyses below.

We extracted the pulsar events in the *NuSTAR* observations in a $30''$ radius circle in the 3–79 keV band, barycenter-corrected the events using R.A.=$15^{\rm h}13^{\rm m}55^{\rm s}.52$, Decl.=$-59^\circ08'08''.8$ (J2000, Caraveo, Mereghetti & Bignami 1994) to produce event lists, and divided each observation into three sub-intervals, yielding twelve sub-intervals for the four observations. We performed H test (de Jager et al. 1989) on the event lists to measure the period for the subintervals and fit the period to a linear function to find the spin period and the spin-down rate. The pulsations were measured with very high significance in each subinterval, and the measured period and the spin-down rate were 0.1517290191(14) s and $1.5281(4) \times 10^{-12}$ s s^{-1} for 56450 MJD, respectively. We folded the light curves using the measured period, and show the resulting pulse profile in Figure 1. We used phases 0.7–1.0 for the PWN to minimize the pulsar contamination in all the subsequent *NuSTAR* data analyses in this paper. The other phase interval was used for the pulsar analysis which will be presented elsewhere. We note that there is contamination from the DC emission of the pulsar even in the off-pulse interval. For example, ∼1.6% of the DC counts are expected in a circle of $R = 30''$ at a distance of $60''$ from the pulsar, but much less at larger distances.

3.2. *Image Analysis*

In order to produce energy-resolved PWN images, we first produced a merged *Chandra* image of the five observations in Table 1 using the `merge_obs` tool of CIAO 4.5 in the 0.5–2 keV, 2–4 keV and 4–7 keV bands with bin size 4 pixels (Fig. 2). Note that the central $4''\times4''$ corresponding to the pulsar emission was removed in these images.

For *NuSTAR* observations, we extracted events in the energy bands 3–7 keV, 7–12 keV, 12–25 keV, and 25–40 keV for the off-pulse phase. After the phase selection, the pulsar component is expected to be reduced significantly. The *NuSTAR* absolute aspect reconstruction accuracy on long timescales is $\sim8''$ (90% confidence), which can blur the resulting merged image obtained with the three observations and two modules. Therefore, we aligned the images by registering the pulsar to the known position before phase filtering. Since only one point source (the pulsar) was significantly detected in each observation, we were not able to fully correct the position (e.g., for translation, rotation and scale). We note that the rotational misalignments are measured and corrected with high accuracy (Harp et al. 2010), and a small residual change in scale is not a concern for the spatial scales of our analyses. Therefore, we assumed that the position offsets were caused by pure translations.

In order to produce deblurred images of the *NuSTAR* observations for comparison with the low-energy high-resolution *Chandra* images, we corrected for the exposure and deconvolved the *NuSTAR* images with the PSF using the `arestore` tool of CIAO 4.5. We then merged the deconvolved images (see Fig. 2). The number of iterations in the deconvolution process was determined by comparing the deconvolved *NuSTAR* image to the *Chandra* image in a similar band. We chose the energy bands so that the average photon energy weighted by the response and the spectrum in a *NuSTAR* band is similar to that in a *Chandra* band, and used the 3–7 keV and 4–7 keV bands for *NuSTAR* and *Chandra*, respectively.

Using the 2-D images, we produced projected profiles along the jet axis (the south-east to north-west direction) in order to compare the deconvolved 3–7 keV *NuSTAR* profile with the 4–7 keV *Chandra* profile. Here, we filled the pulsar region in the *Chandra* data which were removed above with the average counts of the surrounding pixels. We rotated the images 60° clockwise with the origin being the pulsar position, so that the jet structure lies in the horizontal direction (x-axis). We projected the images in Figure 2 onto the axis along the jet, subtracted background, smoothed the profile over a $25''$ scale, and normalized the scale with respect to the brightest point at the center. The backgrounds were assumed to be flat over the detector chips. The background normalization factor was first determined by taking a box in a source-free region, and then further adjusted by matching the y-projected profiles of the source and the background at large distance from the center for each energy band. We found that the results presented below are not sensitive to the background subtraction since background accounts for only small fraction of the intensity. We find that *NuSTAR*-measured profile in the 3–7 keV band is similar to that measured with *Chandra* in the 4–7 keV band (see dashed and dot-dashed curves in fig. 3), and that the results of the deconvolution are not very sensitive to the number of iterations (e.g., 15–50), and we used 20 iterations.

While the deconvolved *NuSTAR* image (Fig. 2e) shows similar overall morphology to the high-resolution *Chandra* image in the similar band (Fig. 2d), there are differences. Most notably, the small arc-like structure and the elongation in the central region ($R \lesssim 30''$) are not resolved in the *NuSTAR* images. This is because the structures are smaller than the FWHM ($\sim18''$) of the *NuSTAR* PSF. Also note that RCW 89, ∼6–7′ north, is not clearly visible in the *NuSTAR* data. This is mainly because the *NuSTAR* observations did not have much exposure in that region; most of RCW 89 fell outside the FoV during the observations.

To measure the size of the narrow structures around the pulsar, we projected events between $-50''$ and $50''$ in the y-axis direction onto the x-axis in several energy bands. The profile is very asymmetric and is not smooth on large scales ($R \gtrsim 100''$). Furthermore, the deconvolution produces artificial structures in the outer regions due to the paucity of counts. Therefore, defining a size (e.g., full width 1% maximum) is impractical on a large scale. However, the source images are smooth on smaller scales ($R \lesssim 50''$), allowing us to measure the FWHM and HWHM in the northern and the southern directions of the projected profiles in several bands without smoothing the images. We measured the sizes by calculating the relative brightness with respect to the peak, and show them in Figures 4a–c. Although there are different structures in the northern and the southern directions, the HWHM's are similar to each other and to half the FWHM.

We calculated the spectrum- and response-weighted average energy for each energy band, fit the widths to a power-law function $R(E) = R_0 E^m$ as suggested by Reynolds (2009), and measured the decay index m for various y-integration widths (e.g., ∼40–130″). The measured decay index was stable over this range, as shown in Figure 4d. Note, however, that our measurement is based on deconvolved images, and our uncertainties are therefore approximate.

3.3. *Spectral Analysis*

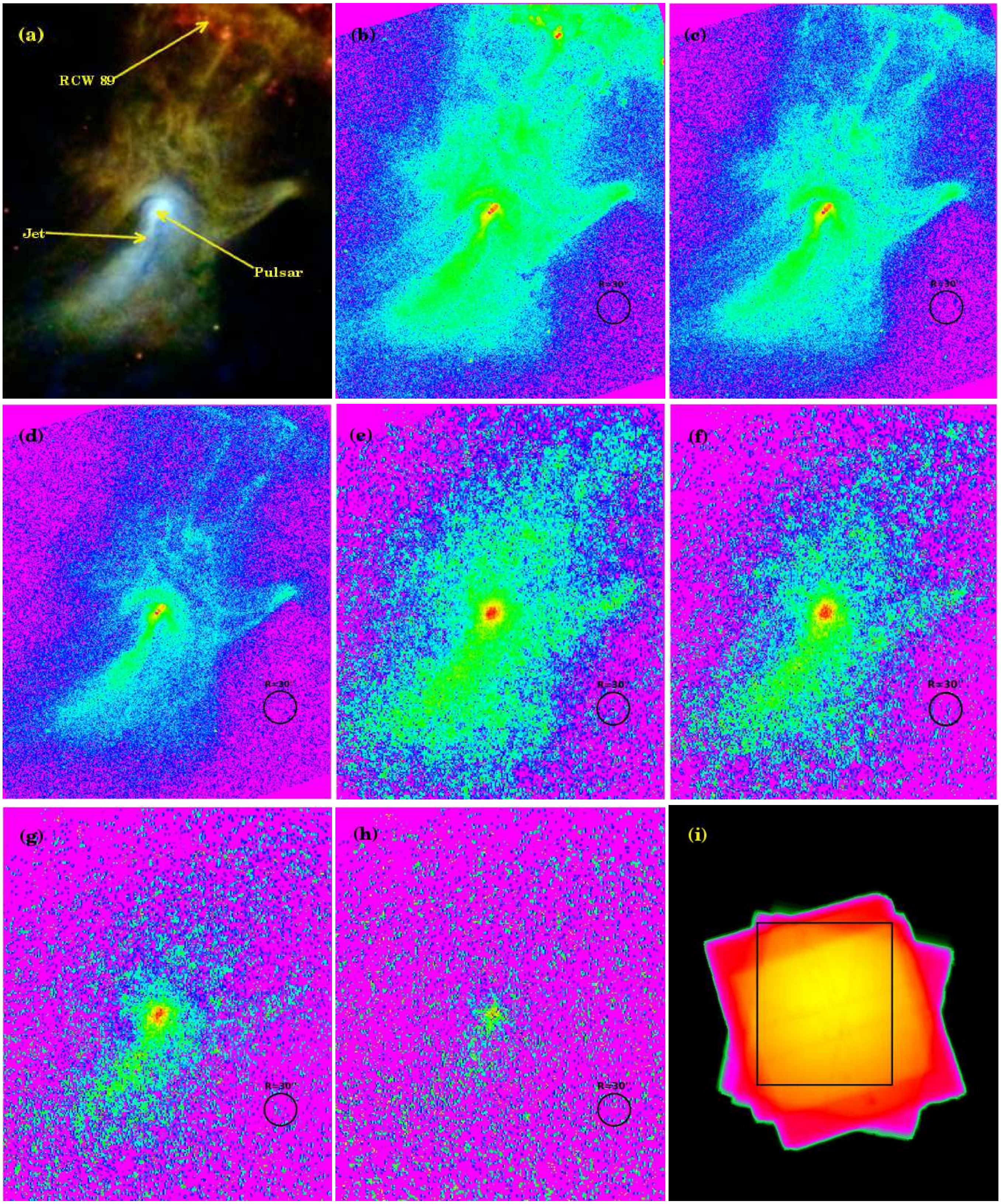

Figure 2. MSH 15−52 images measured with *NuSTAR* and *Chandra* in a $10' \times 12'$ rectangular region: (*a*) A *NuSTAR* and *Chandra* combined false-color image in the 0.5–40 keV band (see http://www.nustar.caltech.edu/image/nustar140109a), and intensity maps (b–h) of (*b*) *Chandra* 0.5–2 keV, (*c*) *Chandra* 2–4 keV, (*d*) *Chandra* 4–7 keV, (*e*) *NuSTAR* 3–7 keV, (*f*) *NuSTAR* 7–12 keV, (*g*) *NuSTAR* 12–25 keV, (*h*) *NuSTAR* 25–40 keV, and (*i*) *NuSTAR* exposure map and a box corresponding to the images. For the *NuSTAR* data, we used off-pulse time intervals only in order to minimize the effect of the central pulsar PSR B1509−58. Exposure and vignetting corrections are applied to the images. A circle with radius $30''$ is shown in panels b–h in black for reference. Note that the images use a logarithmic scale, and each image has a different background level.

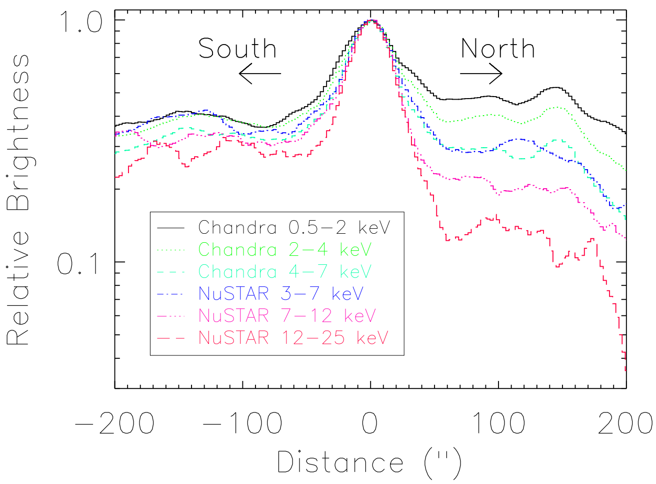

Figure 3. Projected profiles at several energy bands. The profiles are obtained by projecting the images in Fig. 2 onto the jet axis and smoothing over 25″.

The image analysis shows a spectral change with radius in the PWN, and we therefore tried to see differences in spectra at different radii. We extracted spectra in various regions as described, and backgrounds from source-free regions, and fit them with an absorbed power-law model.

Since spatial blurring due to the PSF size is much more significant for *NuSTAR* than *Chandra*, we did not attempt to fit the spectrum jointly except for one case of using a large aperture (Section 3.3.1), where PSF "blurring" is not a large effect. However, we jointly fit the spectra taken with single telescope at different epochs.

We used the χ^2 and the `lstat` statistics in `XSPEC` 12.8.1 to fit the spectra (Arnaud 1996). Results from the two methods were consistent, and we primarily report the results obtained with the χ^2 statistics. Since the *NuSTAR* data are not sensitive to the hydrogen column density ($N_{\rm H}$) and the results are not affected by small change of $N_{\rm H}$, we froze it at a previously reported value (0.95×10^{22} cm^{-2}; Gaensler et al. 2002). We used a cross-normalization factor to account for a slight difference between *NuSTAR* module A and B, and between observations. For the *Chandra* data fitting, we let $N_{\rm H}$ vary and introduced a cross-normalization factor between observations.

3.3.1. *Spectrum of the Entire Nebula*

We first measured the total spectrum of the PWN using a source extraction aperture of R=5′ centered at the pulsar position for a phase interval 0.7–1.0 in the *NuSTAR* data. Photons with energies up to ∼20–30 keV were detected above background for each observation. We extracted a spectrum for this aperture in each of the three *NuSTAR* observations, N1, N3 and N4 in Table 1, and jointly fit the spectra to a power law. The measured power-law index is 2.06 and the absorption-corrected 3–10 keV flux is 5.9×10^{-11} erg cm^{-2} s^{-1} (see Table 2). For the *Chandra* data, we extracted source spectra using the same 5′ aperture, ignoring the central 5″ in order to minimize the pulsar contamination, and jointly fit the five *Chandra* spectra of each region to a power-law model in the 0.5–7 keV band because background dominates above 7 keV. We note that the *Chandra* data fits were not acceptable with χ^2/dof of 2632/2214 ($p = 1\times10^{-9}$), having large residuals in the low energy band below 2 keV. This is perhaps because the large regions are a mixture of subregions with different spectra (e.g., see Section 3.3.4). We therefore fit the data above 2 keV only with frozen $N_{\rm H}$. When removing photons below 2 keV, the remaining data were fit to a single power-law model with a slightly smaller photon index, having χ^2/dof=1757/1704 ($p = 0.18$). The cross-normalization factors for the five *Chandra* observations are all within 1%. Note that letting $N_{\rm H}$ vary also yields an acceptable fit (χ^2/dof=1756/1703) with $N_{\rm H}$=0.91(4) and $\Gamma = 1.90(1)$.

The *Chandra*-measured spectrum in the 2–7 keV band is significantly harder than that measured with *NuSTAR* in the 3–20 keV band. We note that our results are consistent with the previous measurements made with *BeppoSAX* and *INTEGRAL* (Mineo et al. 2001; Forot et al. 2006). Mineo et al. (2001) reported a photon index of 1.90(2) in the 1.6–10 keV band for a 4′ aperture, which is consistent with our *Chandra* measurement in the 2–7 keV band. In the hard band, the reported photon indices were 2.1(2) and 2.12(5) for *BeppoSAX* (20–200 keV) and *INTEGRAL* (15–100 keV), respectively. Note that the large apertures used for *BeppoSAX* and *INTEGRAL* include the RCW 89 region, but the effect of RCW 89 is negligible because the emission is very soft (Yatsu et al. 2005) and the telescopes operate only above 15 keV. The photon index we measure with *NuSTAR* in the 15–30 keV band is 2.1(1) for the 5′-aperture, which agrees with the previous measurements. The results of our measurements are summarized in Table 2.

Since the large apertures include many subregions with different spectral properties as we show below (see Sections 3.3.1, 3.3.3, and 3.3.4), a single power law may not properly represent the combined spectrum. In particular, we find that the best-fit photon index for the *Chandra* data becomes smaller as we ignore lower energy spectral channels, that is, the spectrum appears to harden (is concave up) as we move to higher energies. However, this is the opposite to what we see with *NuSTAR* (Table 2). While this may imply a spectral break in the X-ray band, some other effects such as contamination from the pulsar and/or RCW 89, or cross-calibration systematics between the two instruments may have some impact. Therefore, we investigate some possibilities below in order to see if the discrepancy in the spectral index measurements of *NuSTAR* and *Chandra* is caused by a spectral break.

First, we note that the pulsar contamination was not completely removed in the *Chandra* data. Excising 5″ leaves 2–5% pulsar emission in the $R = 5'$ aperture, which may bias the PWN spectrum. In order to see the effects quantitatively, we fit the pulsed spectrum of the pulsar in the *NuSTAR* data (total spectrum minus the DC level in Fig. 1) with a power-law model and find that the photon index is 1.36(1) and the 3–10 keV flux is $2.24(3)\times10^{-11}$ erg s^{-1} cm^{-2} which broadly agree with the previous measurements (Cusumano et al. 2001; Ge et al. 2012). We added this pulsar component to the *Chandra* fit assuming 5% of the pulsar emission is in the 5′ aperture after the 5″ excision. Thus, the spectral model was a double power-law model, one for the

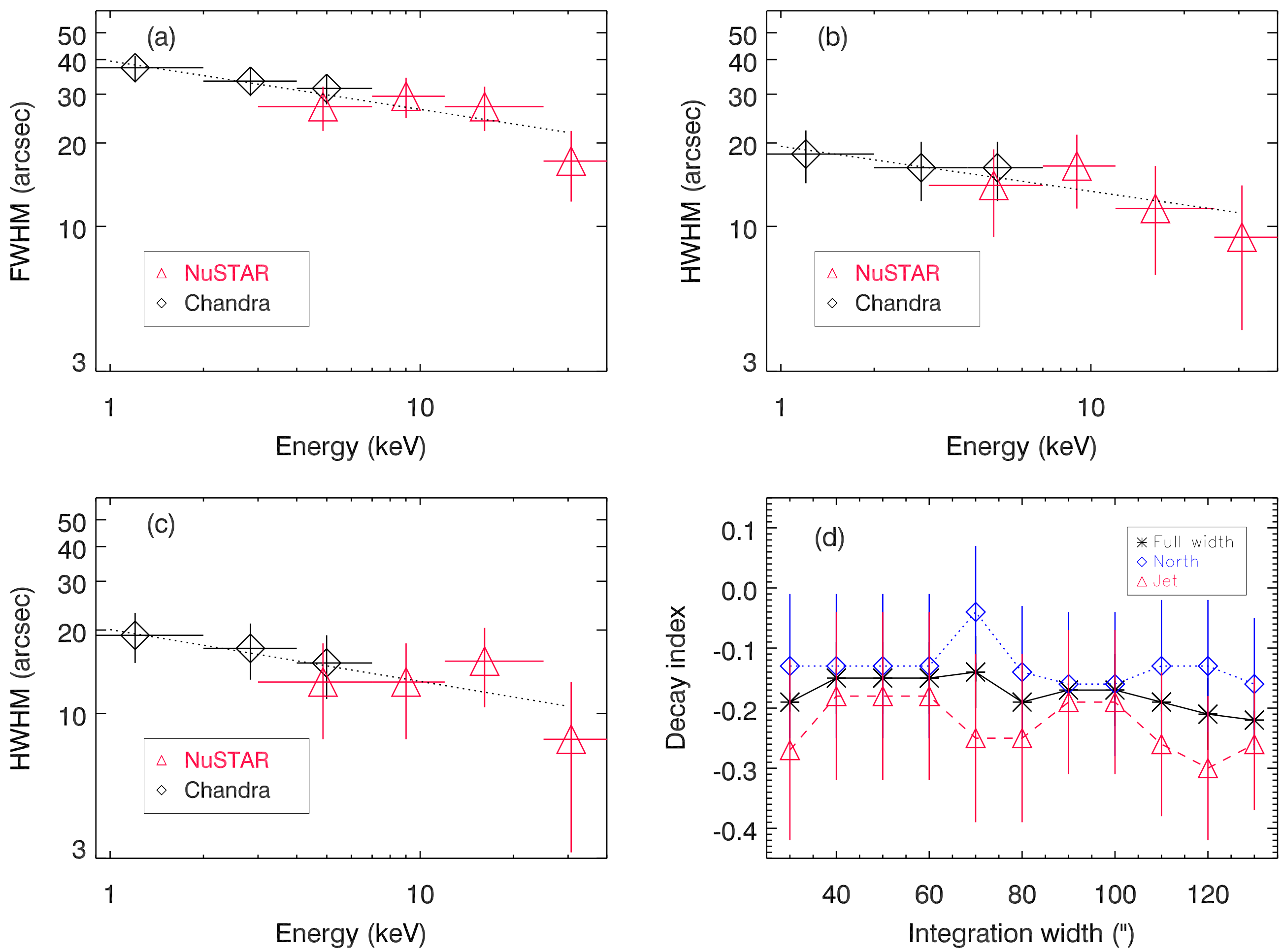

Figure 4. Widths of projected profiles in several energy bands and the best-fit power-law functions, $R(E) = R_0 E^m$, for the FWHM (a), HWHM of the northern (b) and the southern (c) nebulae for a width of 100″, and the decay indices m vs integration widths (d).

pulsar emission and the other for the PWN emission. We froze the pulsar component, fit the PWN spectrum, and find that the spectral index of the PWN does not change. Since the spectral index of the pulsed spectrum may be different in the soft band, we changed the spectral index of the pulsar component to 1.19 as reported by Cusumano et al. (2001) in the 1.6–10 keV band, and find that the photon index of the entire PWN softens only by $\Delta\Gamma = 0.01$. We further increased the pulsar flux by 10% and find no change in the spectral index of the PWN. We verified the results by increasing the excision region to 10″. Note that the DC component of the pulsar is not included in this study. However, the unmodeled DC component is much smaller than the pulsed component as seen in Figure 1, so the effect would be negligible in the *Chandra* data fit.

Second, we consider the effect of the pulsar DC component in the *NuSTAR* data. Although the DC component is negligible in the *Chandra* data due to the image filtering, the DC component presents in the *NuSTAR* data because time filtering does not remove the DC emission. Although it is not possible to measure the DC spectrum accurately, we estimated 3–10 keV DC flux using a 30″ aperture as follows. With *NuSTAR*, we measure the total (pulsed+DC+nebula) and the pulsed flux to be 3.29×10^{-11} erg s^{-1} cm^{-2} and 2.24×10^{-11} erg s^{-1} cm^{-2}, respectively. The nebula flux is measured to be 7.5×10^{-12} erg s^{-1} cm^{-2} with *Chandra* (Section 3.3.3). By subtracting the pulsed and the nebula flux from the total flux, the 3–10 keV DC flux is estimated to be 3.1×10^{-12} erg s^{-1} cm^{-2}. We assumed that the photon index is 1.7, similar to the *NuSTAR*-measured value for the 30″ aperture (Section 3.3.3). We included the DC emission in the *NuSTAR* fit of the 5′-aperture spectrum, and followed the procedure described above for the pulsar contamination estimation in the *Chandra* data. This procedure effectively removes the DC component from the PWN spectrum. However, note that removing such a hard spectrum only softens the spectrum of the entire PWN, making the discrepancy larger. We therefore arbitrarily changed the photon index of the DC component to 2.5 to mitigate the possibility of having very soft DC emission and find that the photon index of the entire PWN hardens only by $\Delta\Gamma = 0.02$.

Third, we varied the background level by $\pm 30\%$, and found that spectral indices change only by 0.02 and 0.01 for *Chandra* and *NuSTAR*, respectively. We also used different background regions and found that the spectral

Table 2
Best-fit parameters for the total PWN emission spectrum

Data[a]	Model[b]	Radius ′	Energy (keV)	N_H[c] (10^{22} cm^{-2})	Γ_s	F_{PL}[d]	E_{break} (keV)	Γ_h	χ^2/dof
C	PL	5	2–7	0.95	1.912(5)	5.98(2)	···	···	1757/1704
C	PL	5	3–7	0.95	1.90(1)	6.00(3)	···	···	1408/1359
N	PL	5	3–7	0.95	2.03(2)	5.93(7)	···	···	543/587
N	PL	5	3–20	0.95	2.06(1)	5.91(5)	···	···	1895/1887
N	PL	5	15–30	0.95	2.1(1)	6.6(1)	···	···	576/579
N + C	PL	5	2–20	0.95	1.950(4)	5.77(5)	···	···	3878/3592
N + C	BPL	5	2–20	0.95	1.918(5)	5.88(5)	6.3(3)	2.12(2)	3691/3590

Notes. 1σ uncertainties are given in parentheses at the same decimal place as the last digit.
[a] N: *NuSTAR*, C: *Chandra*.
[b] PL: `powerlaw` model, and BPL: `bknpower` model in `XSPEC`.
[c] Frozen.
[d] Absorption corrected 3–10 keV flux in units of 10^{-11} erg s^{-1}cm^{-2}.

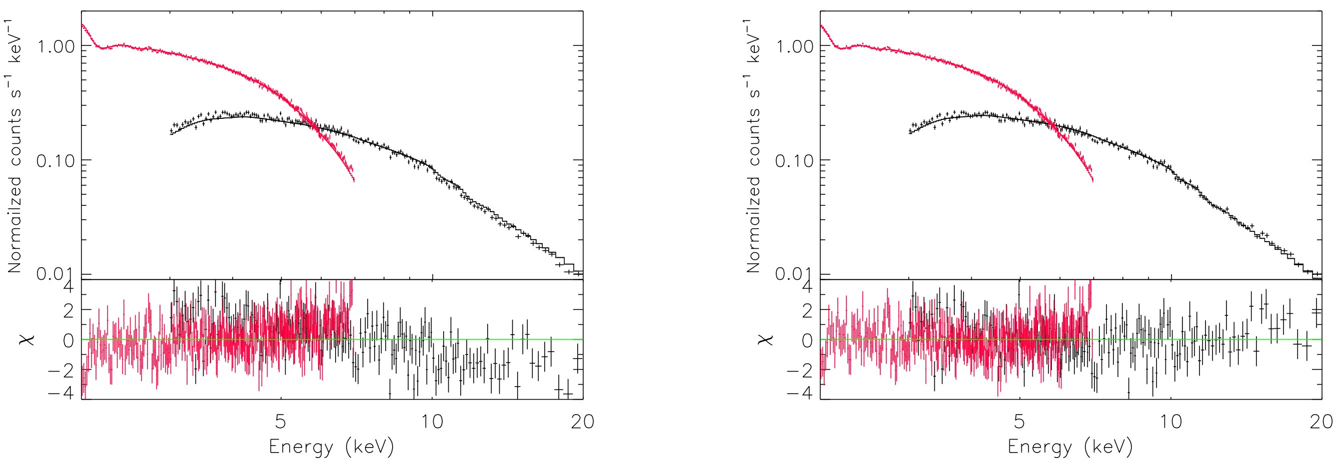

Figure 5. Joint fit results of the *NuSTAR* and the *Chandra* spectra for the single power-law (left) and the broken power-law (right) models. Spectra obtained with each telescope are merged for display purpose only.

indices do not change significantly.

Finally, we estimate the contamination of the RCW 89 emission in the *NuSTAR* data. Using the *NuSTAR* PSF, we estimated the contamination of a structure at $\sim 6'$ into the $5'$ circle to be $\sim$14%. We extracted the RCW 89 spectrum from the *NuSTAR* observation N1 which sampled the RCW 89 best among the *NuSTAR* observations. We added the spectrum as additional background in the PWN spectral fit. Since the other observations N3 and N4 sampled only a small fraction of the RCW 89 region, we used the RCW 89 spectrum extracted from N1 for these observations as well. We varied the normalization of the RCW 89 background from 0.14 to 0.28 in order to account for the fact that the actual RCW 89 region may be larger than what we sampled with *NuSTAR*, and found that the photon index changes by $\lesssim$0.02.

The large discrepancy in the spectral index measurements between *NuSTAR* and *Chandra* cannot be explained by a combination of the above effects. We therefore consider alternatives below. We note that there may be cross-calibration systematics between *NuSTAR* and *Chandra*. For example, Kirsch et al. (2005) showed that systematic uncertainties between X-ray observatories caused by cross calibration are significant using observations of the Crab nebula, for which the authors found that *Chandra* and *BeppoSAX*/LECS measured smaller spectral indices than *BeppoSAX*/MECS and *INTEGRAL* did. Since *NuSTAR* is calibrated so that the spectrum of the Crab nebula is a simple power law with a photon index of 2.1, larger than the *Chandra*-measured value of 1.95 (Kirsch et al. 2005), the spectral break we see for MSH 15−52 could be explained by imperfect cross-calibration.

However, the cross-calibration effects may be different from source to source depending on the spectral shape, and the measurements made for the Crab nebula may not be directly translated into the case of MSH 15−52. We therefore consider an alternative; the discrepancy of spectral indices between the *Chandra* and the *NuSTAR* measurements is caused by a spectral break. We jointly fit the 2–7 keV *Chandra* and the 3–20 keV *NuSTAR* data with a single power law and a broken power law. We find that a single power law does not describe the data well having χ^2/dof=3878/3592 ($p = 5 \times 10^{-4}$), but a broken power law with a break energy of 6.3 keV does (χ^2/dof=3691/3590, $p = 0.12$). The results are presented in Table 2 and Figure 5.

We compared the *NuSTAR* and the *Chandra* spectra in the same energy range below the possible break at 6 keV in order to see if the break is a single sharp break. If so, we expect the *NuSTAR* and the *Chandra* spectra to be same regardless of the difference in the effective area shape. We fit the *NuSTAR* and the *Chandra* spectra in the common energy band, defined as 3–E_{max}, where

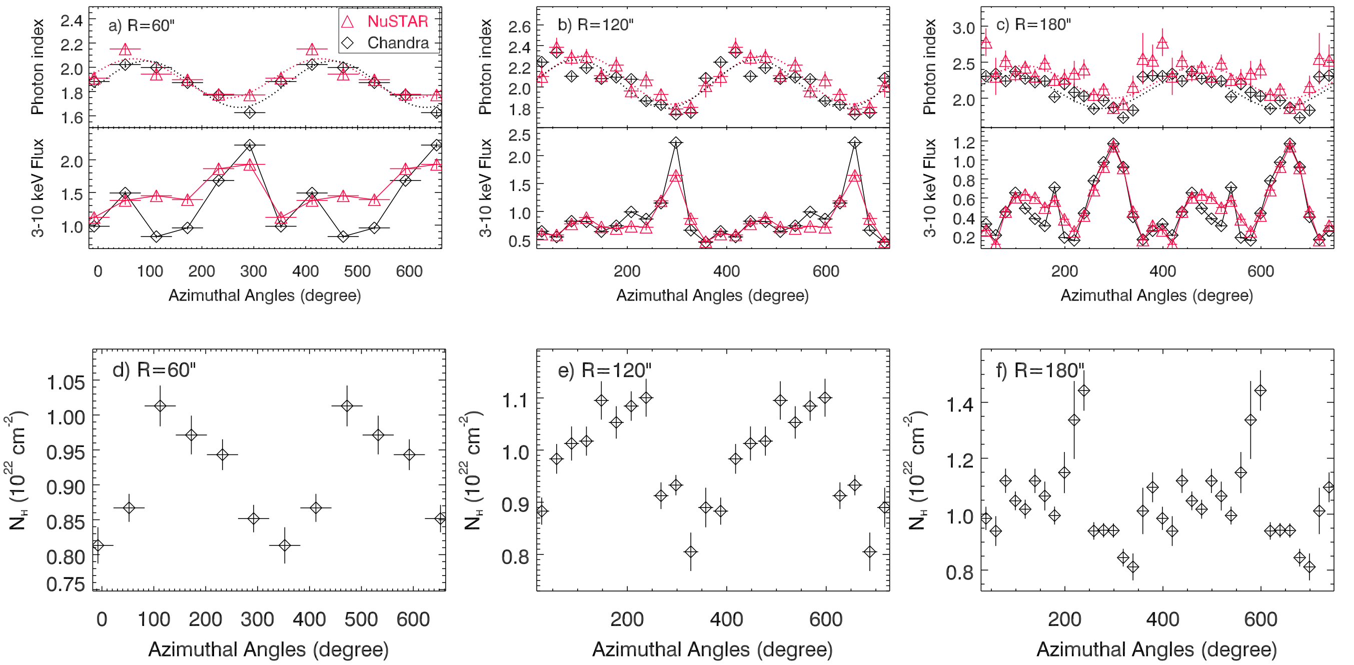

Figure 6. Azimuthal variation of spectral hardness and flux measured with *NuSTAR* (triangles) and *Chandra* (diamonds) at $R = 60''$ (a), $R = 120''$ (b), and $R = 180''$ (c) from the pulsar. Sinusoidal trends for the photon index variation are shown in dotted lines, and solid lines connecting flux data points are shown for clarity. Flux is in units of 10^{-12} erg s^{-1} cm^{-2}. $N_{\rm H}$ values measured with *Chandra* for the same regions are shown in (d)-(f).

we vary $E_{\rm max}$ from 4.5 keV to 7 keV. In the lowest energy band (3–4.5 keV), the *NuSTAR* and *Chandra* results agreed with photon indices of 1.99(7) and 1.98(2). However, as the upper energy range increased to 5 keV and above, the *NuSTAR* results were significantly softer than that of *Chandra*. For example, the photon indices are 2.03(2) and 1.90(1) in the 3–7 keV band, for *NuSTAR* and *Chandra* respectively, inconsistent with each other with 90% confidence. This suggests that the spectral break is likely to be caused by the cross-calibration effect. However, if the spectral break is real, the observational discrepancy in the common energy band may imply that the broadband spectrum is not sharply broken at 6.3 keV but slowly curves over a energy range (e.g., 4–7 keV) probably because different regions in the $300''$ aperture have different break energies. In this case, *NuSTAR* collects relatively more photons above the break than *Chandra* does since it has rising effective area in that band, yielding a softer spectrum.

3.3.2. *Azimuthal Variation of the Spectrum*

In order to see if the PWN spectrum varies azimuthally, we first extracted *NuSTAR* events in $30''$ radius circles for six, twelve, and eighteen azimuth angles for three radial distances, $60''$, $120''$, and $180''$ from the pulsar, respectively. The regions do not overlap. For each region, backgrounds were extracted from an aperture of $R = 45''$ in a source-free region on the same detector chip. We jointly fit the *NuSTAR* spectra for the three observations N1, N2 and N4. The energy ranges for the fit were 3–20 keV, where the source events were detected above the background. We performed these analysis for the same regions with the *Chandra* data in the 0.5–7 keV band.

We show the results in Figure 6, where the azimuth angle ϕ is defined from east in a clockwise direction. A sinusoidal variation of the spectral hardness is clearly visible for each radial group, and the spectrum is hardest in the jet region ($\phi \sim 300°$). The flux values also peak in the jet regions but do not seem to vary sinusoidally. Note there is a small discrepancy between the *NuSTAR* and *Chandra* measurements in Figure 6; the *NuSTAR*-measured spectral indices are larger than those measured with *Chandra* in general. While this may suggest the spectral break we see in the spectrum of entire nebula (Section 3.3.1), it could be due to PSF mixing in the *NuSTAR* data; when there is a sharp spatial contrast such as the jet or image edge, it is convolved with the PSF in the *NuSTAR* data.

It appears that the photon index covaries with $N_{\rm H}$ in Figure 6. We checked if there is a correlation between the two quantities using Pearson's product moments, and found no clear correlation in any radial group.

3.3.3. *Spectral Variation in the Northern Nebula and in the Jet*

Since we observe significant spectral variation in the azimuthal direction, we analyzed the northern nebula and the jet separately. For the northern nebula we used annular regions, ignoring the southern part. Hence, each region covers the upper $\gtrsim 180°$ in azimuth angle. The innermost region was a circle with radius $30''$ centered at the pulsar, and annuli with width $30''$ or $60''$, and boxes were used for the outer regions (see Fig. 7a white). We used the off-pulse phase only for *NuSTAR*, and ignored the central pulsar using a circle with radius $5''$ for *Chandra*.

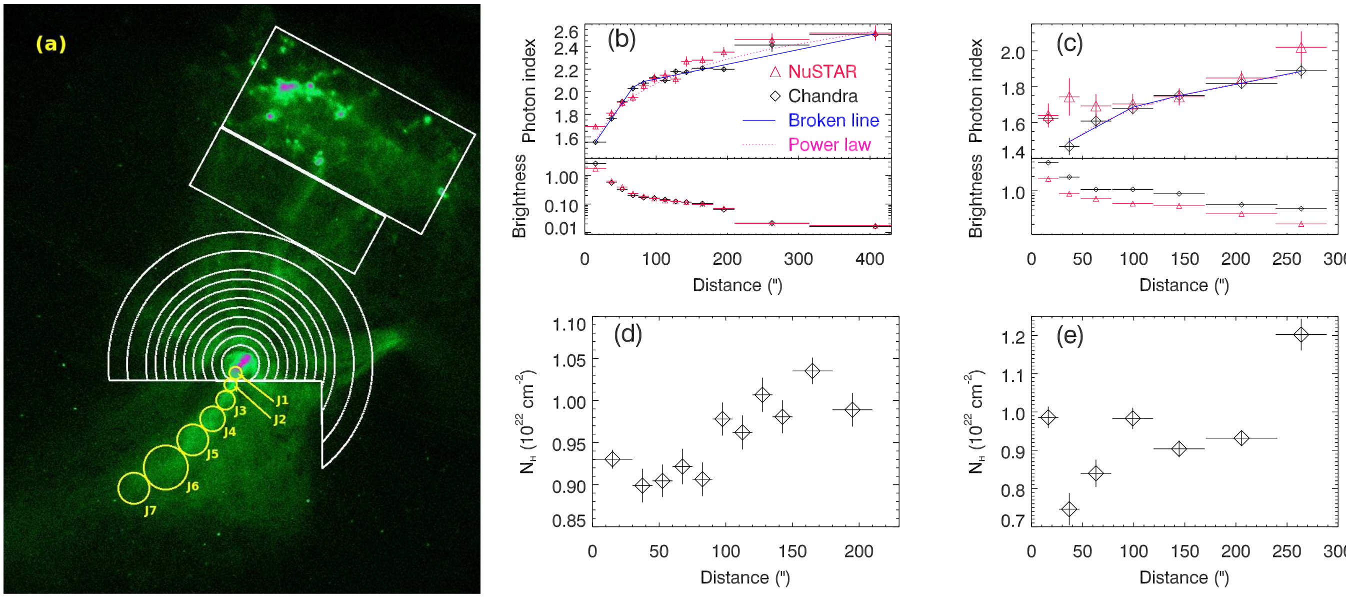

Figure 7. Selected regions for studying the spectral variation in the northern nebula (white annuli and boxes) and in the jet (yellow circles) (a), and spectral variation in the northern and the southern jet directions (b)–(e). Radial variation of the photon indices and surface brightness in the northern nebula (b) and in the jet (c) measured with *NuSTAR* (triangles) and *Chandra* (diamonds). Also shown are the best-fit broken line (blue solid line) and the power law (magenta dotted line). Legends are same for (b) and (c). Brightness is measured in the 3–10 keV band in units of 10^{-15} erg s^{-1} cm^{-2} arcsec^{-2}. Radial profiles of $N_{\rm H}$ measured with *Chandra* are shown in (d) for the northern nebula and in (e) for the jet. Note that the range for the x-axis of (d) is different from that of (b) because $N_{\rm H}$ was not measured for the last two data points in (b).

We separately fit the *NuSTAR* (N1, N2, and N4) and the *Chandra* (C1–C5) spectra of each region with an absorbed power-law model. Since there is significant thermal contamination from RCW 89 in the *Chandra* data at large distances (see the two upper white box regions in Fig. 7a), we ignore the low energy data below ∼3 keV for the two rectangular regions for the *Chandra* fits. We also tried to model the RCW 89 regions using the `vnei` plus a power law in `XSPEC`, and fit the *Chandra* data in the 0.5–7 keV band. The result for the photon index was sensitive to the remnant model but broadly agree with what we found by fitting data above 3 keV only (see also Yatsu et al. 2005). Our results for the *Chandra* data are consistent with, but more accurate than those obtained by DeLaney et al. (2006) who used ∼60 ks of observations taken from 2000 August to 2003 October. We present our measurements in Figure 7b and d.

While our results show that $N_{\rm H}$ increases with radius, we note that it is possible to force the $N_{\rm H}$ to be constant and allow only the photon index to vary. For example, an $N_{\rm H}$ value of $0.957 \pm 0.005 \times 10^{22}$ cm^{-2} constant over the field with photon indices of 1.58–2.16 fits the data out to $R = 200''$ in Figure 7 (χ^2/dof=12289/12363), which implies no radial variation of $N_{\rm H}$ and smaller variation of the photon index with radius. However, the $N_{\rm H}$ profile given in Figure 7d provides better fit with χ^2/dof=12223/12353 corresponding to F-test probability of 2×10^{-10}. We also verified that the results do not change if we fit the spectra only in the 0.5–6 keV (below the spectral break, see section 3.3.1) in order to reduce the effect of the complex continuum. We note that better constraining Γ and $N_{\rm H}$ by jointly fitting the *NuSTAR* data is not possible because of the PSF mixing in the *NuSTAR* data and the spectral break (Section 3.3.1).

There is a hint of a possible break in the linear slope of the radial profile of the photon index $\Gamma(R)$ (Fig. 7b). We measured the location of the break in the northern nebula using a broken line fit. We first fit the *Chandra* measured photon index profile, and found that the break occurs at $R_{\rm break} = 71 \pm 3''$. We note that using a constant $N_{\rm H}$ over the field changes Γ only slightly and gives a consistent result ($R_{\rm break} = 68 \pm 2''$). The *NuSTAR* profile gives a larger $R_{\rm break} = 150 \pm 10''$ because of the large photon index at smaller radii which might be biased by mixing from outer regions. We also find that a single power-law model $\Gamma(R) = \Gamma_0 R^{\eta}$ with $\eta = 0.149 \pm 0.003$ broadly agrees with the data (see Fig. 7b).

Since spectral softening is expected in the jet direction as well, we measured the spectral variation along the southern jet. To do this, we extracted source spectra using non-overlapping circular apertures with radii 10″, 10″, 15″, 20″, 25″, 35″, and 25″ along the jet (see yellow circles in Fig. 7a), which we refer to as regions J1–J7. Note that the center of J1 is $R \sim 15''$ from the pulsar, and all the *NuSTAR* observations (N1–N4) were used for this analysis. We fit the spectra in each region with an absorbed power law, and measured the photon index and flux. The results are presented in Figures 7c and e.

The spectral indices of the J2 region measured with *Chandra* and *NuSTAR* are very different, which may suggest that there is a strong spectral break. However, we note that measuring the spectral parameters with *NuSTAR* was difficult for regions with sharp spectral changes because the *NuSTAR* PSF changes from a circular shape to an elliptical shape with off-axis angle (An et al. 2014), and thus regions with different off-axis angles have different degrees of azimuthal mixing. The four *NuSTAR* observations had different pointings and thus different

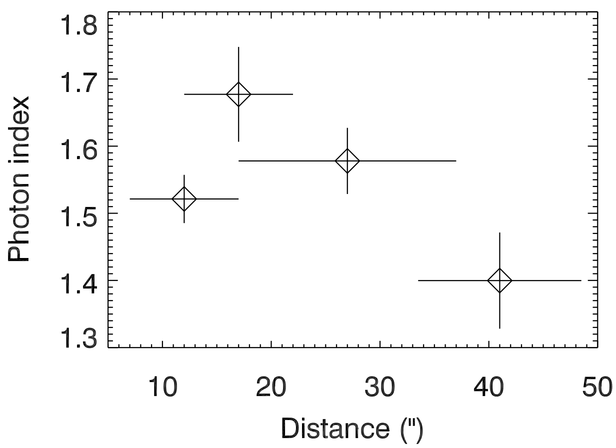

Figure 8. The spectral indices in the central regions, corresponding to the innermost two data points of Fig 7 ($R < 50''$), with a higher spatial resolution.

off-axis and azimuthal angles. In particular, in the regions J1–J2 where we use small apertures and the source spectrum strongly varies, spatial mixing has significant impact on the *NuSTAR* results. Therefore, the discrepancies in the spectral index between the *NuSTAR* and *Chandra* measurements, and even between the *NuSTAR* observations are expected. The mixing was not a concern in the analysis of the northern nebula in which spectral variation is not severe.

We also measured the location of the break in the radial profile of the photon index in the jet direction using the *Chandra* measurement in Figure 7c. Here we ignored the first data point for the reason described below. A fit to a broken line gave a break location of $R_{\rm break} = 110 \pm 30''$. A single power-law model also fits the data with a power index $\eta = 0.12 \pm 0.01$ (Fig. 7c).

We note that the first *Chandra* data point, corresponding to region J1, shows a very soft spectrum compared to the next one in J2, unexpected in synchrotron cooling models (e.g., Reynolds 2003; Tang & Chevalier 2012). The steady-state solutions may not be applicable to the inner region within $\sim1'$ of the pulsar for this source, as DeLaney et al. (2006) found strong variability in the brightness and morphology in that region.

We tried to see if the spectral hardness in J1 varied over time. We first jointly fit the *Chandra* spectra of the region taken from the five observations C1–C5 with a common $N_{\rm H}$, but separate photon index and cross normalization for each observation, and found that the photon indices are all within the 1σ uncertainty of the value in Figure 7. We carried out the same analysis for the J2 region, and found that the spectrum of one observation (C1, Obs. ID 754) was slightly softer than the others ($\Gamma = 1.62 \pm 0.12$) but not significantly. It is probably because the region in this observation fell on the detector chip gap. Therefore, we conclude that the spectral index did not change significantly over time in this region.

Since spectral hardness covaries with $N_{\rm H}$, the spectral difference between the J1 and J2 regions may be less significant if we consider the covariance. In order to investigate the effect of covariance, we ignored Obs. ID 754 because the J2 region in this observation was on the chip gap. We then jointly fit the spectra of each region, varied both $N_{\rm H}$ and Γ using the `steppar` tool in `XSPEC` and found that the 99% contours do not overlap, which suggests that the difference is significant with the covariance as well, and the spectrum of the J1 region is significantly softer than that of the J2 region. If we take the best-fit values, the $N_{\rm H}$ variations of $\sim 3 \times 10^{21}$ cm^{-2} imply extremely high densities of $n \sim 2000$ cm^{-3} for an assumed line-of-sight distance of 0.5 pc (similar to the transverse distance for the assumed distance to the source of 5.2 kpc) in the regions with high $N_{\rm H}$.

We further spatially resolved the J1–J2 regions using overlapping circular regions with radius $5''$. We fit the spectrum of each region with a power-law model, and found spectral softening in the innermost regions ($R \lesssim 20''$). We show the photon indices in Figure 8.

Note that $N_{\rm H}$ increases with radius in the northern nebula. In the jet direction, we used finer spatial resolution, and see a more complicated change; there is a dip at R=30–70$''$. At large distances, we find that $N_{\rm H}$ is large. This structure is visible in the 2-D $N_{\rm H}$ map as well (see Fig. 9). Note also that the power-law index (η) of the photon index profile is larger in the northern nebula than in the jet, that is, the spectral steepening is more rapid, which was also implied by the imaging analysis above (e.g., Fig. 3).

3.3.4. *2-D Maps of the Spectral Parameters*

We produced 2-D maps of the spectral parameters for the $\sim9'\times11'$ field containing the PWN. We used a $1'\times1'$ square region, sliding it over the field with a step of $0.5'$. Thus, two adjacent regions overlap by 50%. Backgrounds were extracted from far outer regions. In order to minimize the pulsar contamination, we excluded a circular region with radius $5''$ for the *Chandra* data, and used the pulse phase 0.7–1.0 only for the *NuSTAR* data.

After extracting 0.5–7 keV spectra in each region for the five *Chandra* observations, we jointly fit the spectra with a common absorbed power-law model having different cross normalization factors between observations and allowing all the parameters to vary throughout. The same procedure was applied to the *NuSTAR* data in the 3–20 keV band with $N_{\rm H}$ frozen to the *Chandra*-measured value in each region. After producing the 2-D maps, we select regions with positive flux with 3σ confidence and show the results in Figure 9. The average (median) of the 1σ uncertainties for the parameters obtained with the *Chandra* data were 1.8×10^{-14} erg cm^{-2} s^{-1} (1.6×10^{-14} erg cm^{-2} s^{-1}), 0.07 (0.05), and 5.6×10^{20} cm^{-2} (3.6×10^{20} cm^{-2}), for flux, photon index, and $N_{\rm H}$, respectively. For *NuSTAR*, the uncertainties were 6.0×10^{-14} erg cm^{-2} s^{-1} (5.8×10^{-14} erg cm^{-2} s^{-1}) and 0.15 (0.12) for flux and photon index, respectively. The flux map shows the structures seen in the count map (Fig. 2). We also note that the photon index map shows the same structure seen in the radial and the azimuthal profiles (Figs. 6 and 7); the photon index increases radially outwards.

We find an interesting shell-like structure in the $N_{\rm H}$ map (top right panel of Fig. 9). Since it is possible that the structure is produced by a correlation between Γ and $N_{\rm H}$, we calculated the correlation coefficient between pairs of parameters using Pearson's product moments. The coefficients were transformed into Fisher coefficients to calculate the significance. In this study, we

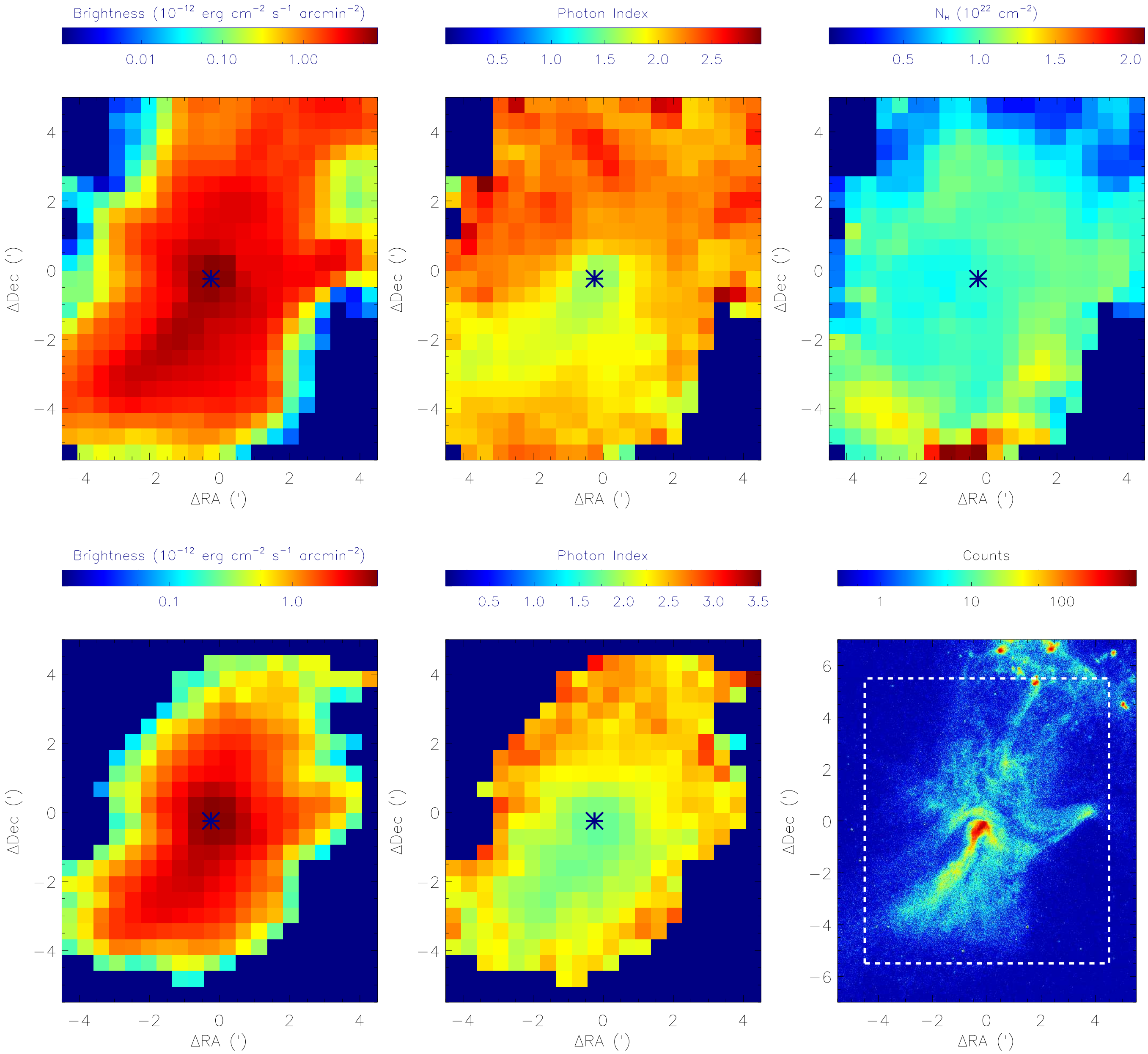

Figure 9. *Top:* 2-D maps of 3–10 keV brightness in units of 10^{-12} erg cm^{-2} s^{-1}arcmin^{-2}, power-law photon index, and $N_{\rm H}$ (from left to right) measured with *Chandra* by fitting the spectra in the 0.5–7 keV band. *Bottom left and middle:* Brightness and photon index measured with *NuSTAR* by fitting the spectra in the 3–20 keV band. *Bottom right: Chandra* counts map and the field for the 2-D maps (white dashed box). The location of the pulsar, PSR B1509−58, is noted with a star except for in the bottom right plot. We arbitrarily assigned zero values to the spectral parameters in regions where the parameters are unconstrained due to paucity of source counts (dark blue regions).

found that the correlation between flux and photon index is −0.58, and the significance is 12σ, implying the correlation is statistically significant. No correlation was found between $N_{\rm H}$ and Γ or any other combination of parameters.

We further tried to fit the *Chandra* data with a single $N_{\rm H}$ value of 0.95×10^{22} cm^{-2} for the entire nebula, and found that the fits became worse, having average χ^2 per average dof of 555/547 compared to the value of 538/546 for the fit with variable $N_{\rm H}$. The single $N_{\rm H}$ fit turned the large $N_{\rm H}$ regions into spectrally hard regions which are not visible in the *NuSTAR* map. However, we note that quantitative comparison with the *NuSTAR* map is difficult unless we know the details of the broadband spectrum in each region.

4. DISCUSSION

We have presented the first hard X-ray images of MSH 15−52 above ∼8 keV. The broadband images show the synchrotron burn-off effect which is asymmetric in space (see Figs. 2 and 3). We find a possible spectral break at $E_{\rm break} = 6$ keV in the spectrum of entire PWN. From the spatially resolved spectral analysis, we found that the spectral index varies sinusoidally in the azimuth direction from $\sim$2 in the north to 1.6 in the south at a distance of $60''$ (1.5 pc) from the pulsar and monotonically increases with distance from 1.6 to 2.5 (Fig. 7). These trends were observed with both *NuSTAR* and *Chandra*. We found that spectral hardness turns over at $R = 35''$ and decreases more slowly beyond $R \sim 60''$ along the jet (Fig. 7), and showed that there is a previously unrecognized shell-like structure of radius $\sim 3'$ in the $N_{\rm H}$ map (Fig. 9).

4.1. *Image*

The *NuSTAR* images in the hard band ($\gtrsim$7 keV, Figs. 2e–h) show that the source shrinks with energy in the 2-D projection on the sky, which is attributed to the synchrotron burn-off effect. While the effect has been shown for this source in a previous study of azimuthally integrated spectra (Schöck et al. 2010), this is the first time it is shown with a 2-D imaging analysis over a broad X-ray band. In particular, we found that the burn-off effect is stronger in the northern direction than in the jet direction (Fig. 3). Although it is very difficult to build a full 2-D model that can reproduce the measured images, matching overall morphological changes in energy may give us important clues to understand particle outflow in the PWN.

The change of the size with energy can be used for inferring properties of the particle flow in the PWN using theoretical models (Kennel & Coroniti 1984; Reynolds 2009). For example, the results of Reynolds (2009) can be rewritten in a form appropriate for sources whose spectral break Δ between radio and X-ray power laws, and size index m can both be measured:

$$\frac{\Delta}{(-m)} = \left(\frac{1}{\epsilon}\right)(1 + 2\epsilon + (3 + 2\alpha_r)m_\rho/3 + (1 + \alpha_r)m_b),$$

where m_x is the index of an assumed power-law function for a quantity $x \propto R^{m_x}$ ($x = \rho$ or b for mass density and magnetic-field strength, respectively), α_r is the energy index of the radio spectrum, and ϵ is a confinement parameter (e.g., $\epsilon = 1$ for conical jets, Reynolds 2009). For the values we derive for MSH 15−5*2* of $\alpha_r = 0.2$, $\Delta = 0.86$, and $m = -0.2$ (Section 3.2), the formula gives

$$1 + 1.1m_\rho + 1.2m_b = 2.3\epsilon.$$

This condition requires either that the mass in the flow is not constant (for instance, due to mass evaporated from thermal gas filaments joining the outflow; Lyutikov 2003), or that magnetic flux is not conserved (for instance, due to turbulent amplification or reconnection): either m_b or m_ρ, or both, must be positive. Various combinations of gradients can reproduce our results. For instance, a conical flow $\epsilon = 1$ requires $1.1m_\rho + 1.2m_b = 1.3$, approximately met if density is constant and magnetic field rises as radius – or vice versa. A confined flow with $\epsilon = 0.44$ (roughly parabolic) would have $m_\rho \cong -m_b$, which could be satisfied with both constant density and constant magnetic field, or with one dropping as fast as the other increases.

4.2. *Spectra of the Entire PWN*

We find that the integrated spectrum of the entire nebula measured with *NuSTAR* is a simple power law with photon index 2.06 (Table 2). This is similar to values previously reported based on *BeppoSAX* and *INTEGRAL* data ($\Gamma = 2.08 \pm 0.01$, 2.12 ± 0.05; Mineo et al. 2001; Forot et al. 2006). The *Chandra*-measured parameters for a single power-law model above 2 keV imply a harder spectrum than that measured with *NuSTAR* (see Table 2), which is also seen in the spectra extracted for other inner regions (e.g., Figs. 6 and 7). We note that our *Chandra* spectral fit results are consistent with that measured previously with *BeppoSAX* ($\Gamma = 1.90 \pm 0.02$ in the 1.6–10 keV band for a $4'$ aperture, Mineo et al. 2001).

Since the large aperture include many subregions with different spectral parameters, we expect to see a harder spectrum at high energies if the spectra of the subregions are simple power laws in the 0.5–20 keV. However, the 3–20 keV *NuSTAR* spectra are much softer than the *Chandra* spectra, which is the opposite to what is expected from a sum of simple power-law spectra. We find that contamination of the pulsar and the backgrounds can explain only $\sim$ 0.01 of the photon index discrepancy of the *NuSTAR* and *Chandra* measurements, while the measured difference is 0.15. The correction for the pulsar, the RCW 89 contamination and the background variation in the data seem not to explain the discrepancy between the *NuSTAR* and the *Chandra* results.

We find that the discrepancy between the *NuSTAR* and the *Chandra* measurements is likely to be caused, at least in part, by imperfect cross calibration of the instruments. However, if the break is real, it implies a break in the energy distribution of the shock accelerated electrons at $\sim$200 TeV (having the peak synchrotron power at 6 keV) for a magnetic field strength of 10 μG, assuming synchrotron emission (e.g., Equation 5 in TC12).

We note that a spectral break in the X-ray band has recently been reported for G21.5−0.9 (Nynka et al. 2014) and the Crab Nebula (Madsen et al. 2014) and may be common to other young PWNe as well. If true, this has important implications on the particle acceleration mechanism in PWNe. Sensitive broadband X-ray observations of other PWNe will be helpful.

4.3. *Spectral Variation*

Using the broadband X-ray data obtained with *NuSTAR* and *Chandra*, we find an azimuthal variation of the spectral index. For the PWN 3C 58, Slane et al. (2004) suggested a possible azimuthal variation of the spectral hardness based on a scenario where current flows out from the pulsar's pole and returns in the equator (Blandford 2002). However, Slane et al. (2004) did not find an obvious azimuthal variation in the PWN 3C 58 within $R \sim 2$ pc for a distance 3.2 kpc we find for MSH 15−5*2* at R=1.5–4.5 pc. Furthermore, we find the azimuthal spectral variation in MSH 15−5*2* is likely sinusoidal and different from that of the flux. This azimuthal spectral variation of the emission may hint at a large scale current flow, however, it could also be due to azimuthal diffusion of jet particles in MSH 15−5*2*.

A radial change of the spectral index of MSH 15−5*2* was reported by Schöck et al. (2010). While they integrated the spectrum over the full azimuthal angle, we measured the profiles for the northern and the jet directions separately because the two regions are different.

We found that significant softening with radius is seen in both directions, more significantly in the northern region. Interestingly, the radial profile of the photon index (rate of spectral steepening) flattens with radius as is also seen in 3C 58 (Slane et al. 2004).

An outflow model considering both diffusion and advection was developed by Tang & Chevalier (2012) (TC12 hereafter), where they calculated the change of the spectral index with distance from the central pulsar with an assumed electron injection spectrum and diffusion coefficient, and were able to reproduce the radial variation of the spectral index for three compact PWNe, the Crab nebula, G21.5−0.9, and 3C 58. The model has been applied to PWNe where the particle escape times (the times for particles to diffuse a distance R in the Bohm limit), are longer than their ages (Equation 2 in TC12):

$$t_{\rm esc} \approx 16,000 \left(\frac{R_{\rm PWN}}{2\ {\rm pc}}\right)^2 \left(\frac{E_e}{100\ {\rm TeV}}\right)^{-1} \left(\frac{B}{100\ \mu{\rm G}}\right)\ {\rm yr},$$

where $R_{\rm PWN}$ is the radius of the PWN, E_e is the energy of synchrotron emitting particles, and B is the magnetic-field strength in the PWN. Using the size $R \sim 10$ pc, E_e = 100–600 TeV (Forot et al. 2006; Nakamori et al. 2008), and an estimation of the magnetic-field strength of 8–17 μG (Gaensler et al. 2002; Aharonian et al. 2005), we find that $t_{\rm esc}$ is 5000–7000 yr, greater than the spin-down estimated age of τ_c = 1700 yr. Since the photon spectrum we are using in this work corresponds to a smaller E_e, $t_{\rm esc}$ can be larger than the above estimation. However, we note that there have been suggestions that the true age of the PWN is $\gtrsim 6000$ yr based on the association with RCW 89, larger than the spin-down estimation (e.g., Seward, Harnden, & Murdin et al. 1983). If so, there may be particles escaping the PWN and the particle spectrum in the outer parts of the PWN becomes steeper, which may be the case for old ($\gtrsim 10^5$ yr) PWNe. For young PWNe, TC12 uses a reflecting boundary condition at the outer edge of the PWN. We note that the TC12 model is for spherically symmetric PWNe and may not be optimal for MSH 15−52. However, the azimuthal variation in the northern nebula is not large (see Fig. 6), and thus the model may provide a reasonable description of the source in that region.

In this model, the angular size of the 'flat' region where the radial profile of the spectral index is flat can be used to estimate the diffusion coefficient (Equation 14 of TC12). This is calculated using the following equations:

$$\theta_{\rm flat} \approx \theta \left(\frac{6^{1/2}}{2}\left[\frac{\nu_R}{\nu}\right]^{1/4} - 1\right)$$

and

$$\nu_R = 1{\times}10^{17} \left(\frac{D}{10^{27}\ {\rm cm^2\ s^{-1}}}\right)^2 \left(\frac{1\ {\rm pc}}{R_{\rm PWN}}\right)^4 \left(\frac{100\mu{\rm G}}{B}\right)^3\ {\rm Hz},$$

where $\theta_{\rm flat}$ is the angular size of the region that has a flat photon index profile, θ is the angular size of the PWN, ν is the photon frequency, and D is the diffusion coefficient.

We find that photon index profile steepens more slowly beyond $R = 71''$ and $R = 110''$ in the northern and the jet regions, respectively. Note that the radial profile of the spectral index in the northern nebula shows a flat region between $R = 70''$–$200''$ although the profile seems not to show any flat region in the southern nebula. We use the value for the northern nebula for the size of the flat region of TC12. Assuming the size of the source is $R_{\rm PWN} \sim 300''$ and using the above formulae with $\nu = 2.4 \times 10^{17}$ Hz (1 keV), we estimated the diffusion coefficient to be 4–13$\times 10^{27}$ cm^2 s^{-1} for B=8–17 μG, which is slightly larger than that estimated for 3C 58 by numerical modeling (2.9×10^{27} cm^2 s^{-1}, TC12).

Using the diffusion coefficient we estimated above, we calculate the critical particle energy $E_{\rm R}$ for which the diffusion distance is equal to the size of the PWN (see Table 3 of TC12) and where the electron distribution has a break (Gratton 1972), using formulae given by TC12: $R = (4D/QE_R)^{\frac{1}{2}}$ and $Q = 1.58 \times 10^{-3} B^2$ erg s^{-1}. For MSH 15−52, we find E_R to be 130–190 TeV for B=8–17 μG. It is interesting to note that this is similar to the maximum electron energies inferred from broadband SED modeling (130 or 250 TeV; Nakamori et al. 2008), and that inferred from the possible spectral break at 6 keV we measured in Section 3.3.1.

We note that the spectrum in the jet direction is significantly softer in the innermost J1 region compared to that in the farther J2 region. Such behavior is not expected in simple advection and/or diffusion models, since the synchrotron emitting particle spectrum only softens with distance. This simple picture may not be appropriate in the regions where the particle flow may be more complicated due to magnetic hoop stress as suggested for this source by Yatsu et al. (2009). The authors found a ring-like structure with $R \sim 10''$ using *Chandra* data and interpreted the structure as the termination shock for this PWN. Based on the morphology, the authors further suggested that the shock accelerated particles are diverted and squeezed towards the poloidal direction right below the ring due to magnetic hoop stress (e.g., Lyubarsky 2002). We also find that the jet structure becomes narrower to $R \sim 35''$ and then broader. Furthermore, the spectral hardness turn-over, non-monotonic variation of the spectral index (see Fig. 7), happens near the location where the jet is narrowest, which might be occurring because of the compression of the magnetic fields and particles.

4.4. *The 2-D Spectral Maps*

We presented 2-D maps of the spectral parameters. The maps visualize the properties of the source very well, and can be compared with 3-D PWN models.

We showed that the 2-D map of $N_{\rm H}$ has a shell-like structure. The density is low near the central pulsar, increasing out to $R \sim 3'$ (see also Figs. 6 and 7). We note that the fit value of $N_{\rm H}$ could in principle be degenerate with other spectral parameters. However, we do not find clear evidence of correlation between $N_{\rm H}$ and photon index or flux from our analysis (see Section 3.3.4), and using a constant $N_{\rm H}$ degrades the fit significantly.

A higher column density is observed in the south and the east directions (see Fig. 9). If the material responsible for $N_{\rm H}$ was produced by the supernova, one would expect the pulsar to have a kick in the opposite direction of the material, towards the north-east direction, which is consistent with the direction of the kick velocity for PSR B1509−58 estimated by Rots (2004) based on 2800 days of timing. However, Livingstone & Kaspi (2011) found no evidence of proper motion using 28 years of timing data. Nevertheless, we do not see any enhanced emission in the shell-like structure, which makes the supernova ejecta scenario less plausible.

Alternatively, the structure may be an interstellar bubble produced by the stellar wind of the supernova progenitor (e.g., Castor, McCray & Weaver 1975). In the wind model, the size of the bubble is given by a simple formula:

$$R_s(t) = 28 \left(\frac{\dot{M}_6 V_{2000}^2}{n_0} \right)^{1/5} t_6^{3/5} \text{ pc},$$

where $\dot{M}_6$ is the mass loss rate of the progenitor in units of $10^{-6} M_\odot \text{yr}^{-1}$, V_{2000} is the speed of the wind in units of 2000 km s^{-1}, n_0 is the number density (cm^{-3}) of the interstellar medium, and t_6 is the time in units of 10^6 yr. The radius of the ring structure we observe is $\sim$5 pc, much smaller than the calculated value for a typical O6 star. However, the value can vary significantly for different input parameters, and due to spatial non-uniformity of the interstellar medium or radiative loss (e.g., Weaver et al. 1977).

The asymmetric shell structure may be explained by outbursts of massive stars. The massive star progenitors of core-collapse supernovae undergo a variety of instabilities that drive episodic mass loss: e.g., pulsations driven by bumps in the continuum opacity (Lamers & Nugis 2002; Fryer, Rockefeller & Young 2006; Paxton et al. 2013) and explosive shell burning (Quataert & Shiode 2012; Arnett, Meakin & Viallet 2014). These outbursts occur up until the collapse of the star and are believed to have large asymmetries. An outburst a few thousand years prior to collapse could explain the features we observe at 5 pc in the remnant.

If, as suggested above, the shell-like structure at R$\sim 3'$ was formed by the stellar wind, the structure would have to avoid being swept up or destroyed by the SN ejecta. If the supernova ejecta did not fill a full spherical shell, a part of the wind-produced shell can be left over. In this case, density of the shell is expected to be higher in the direction where the supernova ejecta were less dense. We see such a trend when comparing our $N_{\rm H}$ map with the radio image of the SNR (Figs. 2 and 3 of Gaensler et al. 1999); there are more ejecta in the northern region than in the southern region.

We have estimated the mass of hydrogen contained in the observed shell-like structure. Using the measured radial profile of $N_{\rm H}$ shown in Figure 7d, the excess mass compared to the central region is $\sim 460 M_\odot$, large compared to the $\sim 12 M_\odot$ one would estimate for a sphere with $R = 5$ pc for typical interstellar density of 1 cm^{-3}. Furthermore, the large amount of material in the structure should produce HI emission, which we do not see in the 20 cm map (Fig. 4 of Gaensler et al. 1999). This may be because the radio continuum emission was not subtracted in the radio map and/or because the X-ray measurement is sensitive only to foreground material while the radio observations are sensitive to both foreground and background structures.

We note that we cannot unambiguously rule out the possibility of a constant $N_{\rm H}$ over the field; the observed $N_{\rm H}$ being an artifact of a more complex underlying continuum. Thus, it is very difficult to clearly interpret the structure using X-ray observations only. Nevertheless, if the shell-like structure in the $N_{\rm H}$ map is intrinsic to the source, it may support the idea of the existence of an underdense region around the supernova progenitor, which was suggested to explain the discrepancy between the pulsar's characteristic age of $\sim$1700 yr (Kaspi et al. 1994) and the SNR age of >10000 yr based on the RCW 89 association (Seward, Harnden, & Murdin et al. 1983). This requires further confirmation by observations in other bands.

5. SUMMARY

We have presented energy-resolved images of the PWN MSH 15−52 in the hard X-ray band ($E > 8$ keV) for the first time. The images in different X-ray bands shrink with energy as a result of the synchrotron burn-off effect. On small scales ($R \lesssim 50''$), we show that the size shrinkage with energy can be explained with a particle advection model. Using this model, we discuss properties of the wind outflow in the jet direction. We find that the combined *NuSTAR*/*Chandra* spectrum of the entire PWN requires a break at 6 keV, which may be due to cross-calibration effects. However, if the spectral break is intrinsic to the source, it implies a break in the shock accelerated electron distribution. We measured the spectral index profiles on large scales ($R \sim 5'$) in the northern and jet directions. The spectrum softens with radius in both directions, an effect we interpret with a combined diffusion/advection model; further numerical simulations with the model are required for more accurate interpretation. We find an interesting sinusoidal variation of the spectral hardness in the azimuthal direction which may have implications for the particle diffusion in the PWN. Such a variation has not been seen in other PWNe, though it has been predicted in pulsar current flow models (Blandford 2002). We find a spectral hardness turn-over in the jet direction at a distance of $\sim 35''$ from the pulsar. Finally, we presented 2-D maps of spectral parameters of the source, and find that the $N_{\rm H}$ map shows an interesting shell-like structure which implies high particle density. However, this feature could result from a complex underlying continuum, and so requires further confirmation.

This work was supported under NASA Contract No. NNG08FD60C, and made use of data from the *NuSTAR* mission, a project led by the California Institute of Technology, managed by the Jet Propulsion Laboratory, and funded by the National Aeronautics and Space Administration. We thank the *NuSTAR* Operations, Software and Calibration teams for support with the execution and analysis of these observations. This research has made use of the *NuSTAR* Data Analysis Software (NuSTARDAS) jointly developed by the ASI Science Data Center (ASDC, Italy) and the California Institute of Technology (USA). V.M.K. acknowledges support from an NSERC Discovery Grant and Accelerator Supplement, the FQRNT Centre de Recherche Astrophysique du Québec, an R. Howard Webster Foundation Fellowship from the Canadian Institute for Advanced Research

(CIFAR), the Canada Research Chairs Program and the Lorne Trottier Chair in Astrophysics and Cosmology.

REFERENCES

Aharonian, F., Akhperjanian, A. G., Aye, K. -M., Bazer-Bachi, A. R., Beilicke, M. & et al. 2005, A&A, 435, L17

An, H., Madsen, K. K., Westergaard, N. J. & et al. 2014, Proc. SPIE, 9144, 91441Q

Arnaud, K. A. 1996, in ASP Conf. Ser. 101, Astronomical Data Analysis Software and Systems V, ed. G. H. Jacoby & J. Barnes (San Francisco,CA: ASP), 17

Arnett, W. D., Meakin, C. & Viallet, M. 2014, AIP Advances 4, 4, arXiv:1312.3279

Atoyan, A. M., & Aharonian, F. A. 1996, MNRAS, 278, 525

Blandford, R. D. 2002, in Proc. MPA/ESO/MPE/USM Joint Astron. Conf., Lighthouses of the Universe: The Most Luminous Celestial Objects and Their Use for Cosmology (Berlin: Springer), 381, arXiv:0202265

Castor, J., McCray, R. & Weaver, R. 1975, ApJ, 200, L107

Caraveo, P. A., Mereghetti, S. & Bignami, G. F. 1994, ApJ, 423, L125

Chevalier, R. A. 2005, ApJ, 619, 839

Cusumano, G., Mineo, T., Massaro, E., Nicastro, L., Trussoni, E., Massaglia, S., Hermsen, W., & Kuiper, L. 2001, A&A, 375, 397

de Jager, O. C., & Harding, A. K., et al. 1992, ApJ, 396, 161

de Jager, O. C., Swanepoel, J. W. H., & Raubenheimer, B. C., et al. 1989, A&A, 221, 180

DeLaney, T., Gaensler, B. M., Arons, J. & Pivovaroff, M. J. 2006, ApJ, 640, 929

Forot, M., Hermsen, W., Renaud, M., Laurent, P., Grenier, I., Goret, P., Khelifi, B., & Kuiper, L. 2006, ApJ, 651, L45

Fryer, C. L., Rockefeller, G. & Young, P. A. 2006, ApJ, 647, 1269

Gaensler, B. M., Arons, J., Kaspi, V. M., Pivovaroff, M. J., Kawai, N., & Tamura, K. 2002, ApJ, 569, 878

Gaensler, B. M., Brazier, K. T. S., Manchester, R. N., Johnston, S. & Green, A. J. 1999, MNRAS, 305, 736

Gaensler, B. M., & Slane, P. O. 2006, ARA&A, 44, 17

Garmire, G. P., Bautz, M. W., Ford, P. G., Nousek, J. A., & Ricker, G. R. 2003, Proc. SPIE, 4851, 28

Gratton, L. 1972, Ap&SS, 16, 81

Ge, M. Y., Lu, F. J., Qu, J. L., Zheng, S. J., Chen, Y., & Han, D. W. 2012, ApJS, 199, 32

Harp, D. I., Liebe, C. C., Craig, W., Harrison, F., Kruse-Madsen, K., Zoglauer, A. 2010, Proc. SPIE, 7738, 77380Z

Harrison, F. A., Craig, W. W., Christensen, F. E., et al. 2013, ApJ, 770, 103

Kaspi, V. M., Manchester, R. N., Siegman, B., Johnston, S., & Lyne, A. G. 1994, ApJ, 422, L83

Kaspi, V. M., Roberts, M. S. E., & Harding, A. K. 2006, in Compact Stellar X-Ray Sources, ed. W. Lewin & M. van der Klis (Cambridge: Cambridge Univ. Press), 279

Kirsch, M. G. F., Briel, U. G., Burrows, D., & et al. 2005, Proc. SPIE, 5898, 589803

Kennel, C. F., & Coroniti, F. V. 1984, ApJ, 283, 710

Lamers, H. J. G. L. M. & Nugis, T. 2002 A&A, 395, L1

Livingstone, M. A., & Kaspi, V. M. 2011, ApJ, 742, 31

Lyubarsky, Y. E., 2002, MNRAS, 329, 34L

Lyutikov, M., 2003, MNRAS, 339, 623

Madsen, K. K., Reynolds, S., Harrison, F. A., & et al. 2014, ApJ, submitted

Mineo, T., Cusumano, G., Maccarone, M. C., Massaglia, S., Massaro, E., & Trussoni, E. 2001, A&A, 380, 695

Mori, K., Burrows, D. N., Hester, J. J., Pavlov, G. G., Shibata, S., & Tsunemi, H. 2004, ApJ, 609, 186

Nakamori, T., Kubo, H., Yoshida, T., Tanimori, T., Enomoto, R., & et al. 2007, ApJ, 677, 297

Nynka, M., Hailey, C. J., Reynolds, S. P., & et al. 2014, ApJ, 789, 72

Paxton, B., Cantiello, M., Arras, P., & et al. 2013, ApJS, 208, 4

Quataert, E. & Shiode, J. 2012, MNRAS, 423, L92

Reynolds, S. P. 2003, in Proc. IAU Colloquium 192, 10 Years of SN1993J, Valencia, Spain, April 2003, arXiv:0308483

Reynolds, S. P. 2009, ApJ, 703, 662

Rees, M. J. & Gunn, J. E. 1974, MNRAS, 167, 1

Rots, A. H. 2004, in AIP Conf. Proc. 714, X-Ray Timing 2003: Rossi and Beyond, ed. P. Kaaret, F. K. Lamb & J. H. Swank (Melville: AIP), 309 http://adsabs.harvard.edu/abs/2004AIPC..714..309R

Schöck, F. M., Büsching, I., de Jager, O. C., Eger, P., & Vorster, M. J. 2010, A&A, 515, A109

Seward, F. D., Harnden, Jr., F. R., Murdin, P., & Clark, D. H. 1983, ApJ, 267, 698

Sironi, L., & Spitkovsky, A. 2009, ApJ, 698, 1523

Slane, P., Helfand, D. J., van der Swaluw, E., & Murray, S. S. 2004, ApJ, 616, 403

Tang, X., & Chevalier, R. 2012, ApJ, 752, 83

Weaver, R., McCray, R., Castor, J., Shapiro, P., & Moore, R. 1977, ApJ, 218, 377

Wilson, A. S. 1972a, MNRAS, 160, 355

Wilson, A. S. 1972b, MNRAS, 160, 373

Yatsu, Y., Kawai, N., Kataoka, J., Kotani, T., Tamura, K., & Brinkmann, W. 2005, ApJ, 631, 312

Yatsu, Y., Kawai, N., Shibata, S., & Brinkmann, W. 2009, PASJ, 61, 129